Climate-driven hydrological change and carbonate platform demise induced by the Paleocene–Eocene Thermal Maximum (southern Pyrenees)

Juan Li[1], Xiumian Hu[1*], Eduardo Garzanti[2], Marcelle BouDagher-Fadel[3]

[1] State Key Laboratory of Mineral Deposit Research, School of Earth Sciences and Engineering, Nanjing University, Nanjing 210023, China

[2] Laboratory for Provenance Studies, Department of Earth and Environmental Sciences, Università di Milano-Bicocca, 20126 Milano, Italy

[3] Department of Earth Sciences, University College London, London WC1H 0BT, UK

Abstract

The Campo section in the Spanish Pyrenees is classical for shallow-water Paleocene/Eocene boundary studies. Despite extensive work in the last decades, the location of the onset of the negative carbon isotope excursion (CIE) which marks the Paleocene-Eocene thermal maximum (PETM), and hence the Paleocene/Eocene boundary, remains a matter of considerable debate. We present here new sedimentological, biostratigraphic, and carbon-isotope data across the Paleocene-Eocene boundary to investigate environmental and sea-level changes across the PETM. The core of the PETM event was identified within the Claret Formation. Foraminiferal assemblages of SBZ4/SBZ5 found below the Claret Formation are replaced by SBZ6 assemblages above. Detailed microfacies analysis indicated that the pre-PETM upper Thanetian limestone represents transgressive inner-ramp deposits, overlain unconformably by mixed carbonate-siliciclastic deposits of the syn-PETM Claret Formation, overlain unconformably in turn by renewed carbonate-ramp deposition in the post-PETM lower Ypresian limestone. The temporary demise of the carbonate ramp during the PETM is ascribed to increased siliciclastic supply associated with a significant change in regional hydrology driven by an increase in magnitude and frequency of extreme rainfall and runoff events. The isotopically defined P/E boundary, does not match the biostratigraphically defined horizon, but would do so if the P/E boundary were to be placed at the end of, rather than at the onset of the CIE.

Keywords: Paleocene/Eocene Thermal Maximum; Climate change; Carbon isotopes; Carbonate ramp microfacies; Siliciclastic supply; Southern Pyrenees.

1 Introduction

The Paleocene–Eocene thermal maximum (PETM; ~56 Ma) was a period of climate change, associated with a large perturbation to the carbon cycle and a global sea-surface temperature rise of at least 4 to 5°C (McInerney and Wing, 2011; Dunkley Jones et al., 2013). In the sedimentary record, the onset of the PETM is marked by a negative carbon-isotope excursion, reflecting the release of large amounts of ^{13}C-depleted carbon to the ocean and atmosphere (McInerney and Wing, 2011) and resulting in global warming (Zachos et al., 2003), ocean acidification (Zachos et al., 2005; Penman et al., 2014), and pronounced impact on marine and terrestrial biota (McInerney and Wing, 2011). The cause and nature of the massive carbon release leading to such an extreme climatic event remain under debate. Arguments for marine methane-hydrate release, volcanic intrusion into organic-rich marine sediments, oxidation of huge amounts of organic carbon, and bolide impact have been put forward (Gutjahr et al., 2017; McInerney and Wing, 2011). Regardless of the cause, the environmental and ecological changes centered on the PETM carbon event are the subject of extensive study, because they provide an imperfect yet useful analog to modern deteriorating conditions related to the ongoing increase in atmospheric carbon dioxide (Zeebe et al., 2016).

Although many PETM sites have been documented in open marine and terrestrial environments, there are still only a few PETM records from shallow-water carbonate ecosystems, which are key locations to link continental and open-marine settings. The lack of records from shallow-water successions is due partly to a scarcity of suitably continuous sections and partly to imprecise temporal constraints. Recent work on Tethyan carbonate platforms in Egypt, northern Spain, and Tibetan Himalaya has documented the response of benthic fauna to the PETM and better identified the position of the Paleocene/Eocene (P/E) boundary based on benthic zones, thus providing new elements to better understand environmental changes during the PETM (Orue-Etxebarria et al., 2001; Pujalte et al, 2003, 2009; Scheibner et al., 2005; Zamagni et al., 2012; Zhang et al., 2018; Li et al., 2017).

The Campo section is a classic shallow -marine PETM locality in the southern Pyrenees and the target of biostratigraphic (Molina et al. 2003; Orue-Etxebarria et al., 2001; Scheibner et al., 2007), chemostratigraphic (Schmitz and Pujalte, 2003; Manners et al., 2013; Duller et al., 2019) and lithostratigraphic investigations (Payros et al., 2000; Schmitz and Pujalte, 2007; Pujalte et al., 2009, 2014). Notwithstanding, the PETM onset and the P/E boundary in the Campo section remain uncertainly defined. We present here a new sedimentological, biostratigraphic, and high-resolution carbonate-isotope analysis of the Campo section to reassess the PETM record, locate precisely the P/E boundary, reconstruct the environmental and sea-level changes across the PETM, and investigate hydrological changes and carbonate-platform response to the PETM abrupt warming.

2 Study area and methods

The Pyrenees are a 400 km-long but relatively narrow (~150 km) fold-thrust belt formed during collision between Eurasia in the north and Iberia in the south (Roest and Srivastava, 1991). During the early Paleogene, the Pyrenean domain was a deep-water gulf opening towards the Bay of Biscay in the west and rimmed by shallow-marine carbonates (Plaziat, 1981; Pujalte et al., 2002). The Campo section (present coordinates N42°23′17.39″, E00°23′52.88″) is part of the Tremp-Graus Basin located in the southeastern margin of the Paleogene Pyrenean gulf (Fig. 1).

From the measured section, over 60 samples were collected to increase the resolution of the existing bulk-carbonate isotope record supplemented by high-resolution biostratigraphic and microfacies analyses.

Microfacies analysis was based on macrofossil and microfossil assemblages, detrital minerals, textures, and structures observed in both thin sections and outcrops. Macrofossil groups including gastropods, echinoderms, calcareous red and green algae, and larger, small, and agglutinated benthic foraminifera were identified and used to interpret the depositional environment according to Wilson (1975) and Flügel (2010). Carbonate and mixed siliciclastic–carbonate rocks were classified based on Dunham (1962), Embry and Klovan (1971) and Mount (1985). The identification of larger benthic foraminifera was based on key morphological characteristics including coiling mode, peripheral shape, arrangement and number of chambers, presence or absence of keels, and sutural properties. All species used in this work represent index fossils of the Tethyan Shallow Benthic Zonation established by Hottinger (1960), revised by Serra-Kiel at al. (1998), and tied to the time scale of Gradstein et al. (2012).

The analysis of stable carbon isotopes in bulk carbonate samples was performed at the State Key Laboratory for Mineral Deposits Research at Nanjing University. Carbonates were analyzed with an in-line GasBench II auto sampler coupled to a Finnigan MAT Delta Plus XP mass spectrometer. Powdered samples were obtained by micro-drilling – taking care to avoid cement-filled veins and pores or bioclasts – and reacted with purified orthophosphoric acid at 70°C. Data are expressed in standard delta notation (δ) as permil deviations from the Vienna Pee Dee Belemnite (VPDB) standard. Duplicate measurements of standards yielded an analytical precision (1σ) of 0.1 and 0.05‰ for $\delta^{13}C$ and $\delta^{18}O$.

3 Results

3.1 Lithostratigraphy

The general sedimentology and stratigraphy of the Campo section are described in detail in Scheibner et al. (2007) and Pujalte et al. (2014), to which the reader is referred. Here we focus specifically on the stratigraphic interval containing the Paleocene-Eocene boundary, which is divided into three lithological units separated by unconformable contacts: upper Thanetian limestone, Claret marls, and Ypresian (Ilerdian) limestone (Pujalte et al., 2014) (Fig. 2A).

The 14 m-thick upper Thanetian limestone comprises mainly thick-bedded gray limestone with diverse species of calcareous red algae and larger benthic foraminifera (Fig. 2B). The unconformable contact with the overlying Claret Formation is marked by a sharp surface containing abundant corals, gastropods, and bivalves (Fig. 2C, 2D).

The 10 m-thick Claret Formation is characterized by greenish-gray marls interbedded with thin- to thick-bedded impure limestone containing siliciclastic detritus (Fig. 2E). Four members are identified (Pujalte et al., 2014): member 1 (~ 6 m) consists of greenish marl interbedded with thin siltstone, member 2 (2-4 m) of channelized pebbly sandstone embedded in mudrock, member 3 (~ 2 m) of siltstone, and member 4 (≤ 1 m) of thick-bedded limestone.

The 15 m-thick lower Ypresian limestone is thin- to thick-bedded and rich in larger benthic foraminifera (Fig. 2F, 2G).

3.2 Biostratigraphy

Thin sections very rich in well preserved larger benthic foraminifera could be firmly correlated with the shallow benthic zones (SBZ) proposed by Serra-Kiel et al. (1998) and BouDagher-Fadel et al. (2015), thus providing robust constraints to the age of the studied strata (Fig. 3, Fig. 4). The presence of *Assilina yvettae*, *A. granulosa*, and *Ranikothalia thalica, Glomalveolina levis* (Fig. 4A), *Rotorbinella skourensis, Miscellanea miscella* (Fig. 4B-C) indicate an SBZ4 age for the lower part of the upper Thanetian limestone. The assemblages of SBZ5 include *Miscellanea miscella*, *Rotospirella conica* (Fig. 4D), *Redmondina henningtoni* and the coralline *alga Distichoplax biserialis* (Fig. 4E). Cretaceous and Early Paleocene reworking is common throughout SBZ5. The presence of inner neritic planktonic foraminifera, e.g. *Planorotalites chapmani* and *Globanomalina planoconica* indicate a deepening of the environment towards the top of SBZ5. The appearance of *Alveolina globula* (Fig. 4G) indicate an SBZ6 age (P5b, 56.0-54.9 Ma) for the lower Ypresian limestone, also containing common *Opertorbitolites gracilis* (Fig.4F), *Alveolina pasticillata* (Fig. 4I), *Alveolina globosa*, *Alveolina aragonensis* and *Operculina* sp. The upper Thanetian limestone is thus assigned to SBZ4 and SBZ5 (between 56.0 and 55.8 Ma), whereas the Ypresian limestone can be constrained to SBZ6 (between 56.0 and 54.9Ma) (Fig. 3).

3.3 Carbonate microfacies

Thirteen microfacies (MF), corresponding to shoal, shallow open marine, paralic and restricted lagoon environments in an inner to middle carbonate ramp setting were identified by integrating sedimentological and paleontological observations (Table 1). A detailed description of the identified microfacies is reported below.

3.3.1 Upper Thanetian limestone

MF1 Sandy red algal packstone/rudstone

Thick-bedded gray packstone/rudstone at the base of the upper Thanetian limestone with abundant bioclasts (coralline algae, larger and small benthic foraminifera, echinoderms) set in micritic matrix (Fig.5A). Abundant quartz grains decrease up-section. Sparite is locally present.

Rock-forming rotaliinid benthic foraminifera characterize restricted to open marine environments in platform interiors and inner ramps (Flügel, 2010). Calcareous red algae indicate the photic zone in platform margins and inner-ramp to mid-ramp settings. MF1 points to restricted marine conditions with sporadic siliciclastic supply in an inner ramp environment above fair-weather wave base and adjacent to shoal bars.

MF2 Foraminiferal/red algal grainstone

Abundant larger benthic foraminifera (mainly *Miscellanea*, *Rotorbinella*, *Operculina,* and *Assilina*) and calcareous algae in sparitic cement are identified in the lower part of the upper Thanetian limestone (Fig. 5B). Echinoderm fragments commonly showing syntaxial rims, intraclasts, and miliolids also occur.

MF2 is similar to MF1 but the occurrence of blocky-calcite content and the absence of siliciclastic particles indicate high-energy shoals above fair-weather wave base (Flügel, 2010).

MF3 Coralline algae bindstone

Thick gray beds in the middle and upper parts of the upper Thanetian limestone contain coralline algae encrusting foraminifera and bryozoans set in micrite (Fig. 5C). Larger and small benthic foraminifera, ostracods, and echinoderm fragments occur.

Micritic matrix reflects a low-energy environment. Encrusting calcareous red algae typically thrive at 30-80 m water depths (Adey et al., 1979). A shallow open marine environment below fair-weather wave base is indicated (RMF12 of Flügel, 2010).

MF4 *Distichoplax* wackestone

Thick gray beds in the upper part of the upper Thanetian limestone are locally dominated by large, unfragmented *Distichoplax* (an enigmatic coralline alga, Sarkar, 2018) set in micrite (Fig. 5D). Fragments of corals, larger benthic foraminifera, echinoderms, and *Microcodium* (a problematic fossil feature formed by biogenic processes in carbonate-rich soils; Košir, 2004; Kabanov et al., 2008) also occur.

Micritic matrix indicates a low-energy environment. *Distichoplax* is interpreted to have thrived in the intertidal to subtidal zone (Sarkar, 2018).

MF5 *Microcodium* packstone

At the top of the upper Thanetian limestone, thick gray beds with sharp erosive base are dominated by *Microcodium* with minor miliolids and intraclasts set in micrite (Fig. 5E, 5F). *Microcodium* generally occurs as disarticulated prisms 0.3-0.5 mm-long and 0.03-0.05 mm-wide; better preserved and nearly complete rosette forms are rare.

Disaggregated and partly degraded *Microcodium* suggests reworking of calcareous paleosols during sudden floods from the continent (Pujalte et al., 2019).

3.3.2 Claret Formation

MF6 Marlstone with sandy rudstone

In the Claret Formation, greenish-gray marls containing quartzose silt and sporadic ostracods and charophyte algae (member 1, MF6a, Fig. 5G) are interbedded with thin- to medium bedded rudstone containing well sorted, subangular to subrounded quartz grains of fine to medium sand size as well as poorly sorted bioclasts and intraclasts (member 2, MF6b; Fig. 5H), and wackestone containing well sorted, subangular to subrounded quartz grains of fine to medium sand size and sporadic small benthic foraminifera (member 3, MF6c; Fig. 6A). *Microcodium*, echinoderm fragments, and small benthic foraminifera are common.

Micritic matrix reflects a low-energy brackish to schizohaline paralic environments affected by terrigenous supply.

MF7 Small benthic foraminiferal wackestone

Thin bedded gray limestones of the uppermost Claret Formation (member 4) contain small benthic foraminifera, rare charophytes, and ostracods set in micritic matrix (Fig. 6B).

Micrite and oligotypic fauna suggest deposition in a low-energy brackish to schizohaline lagoon (Flügel, 2010).

3.3.3 Lower Ypresian limestone

MF8 *Miliolid* packstone

Thin gray beds at the base of the Ypresian limestone contain abundant miliolids set in micrite (Fig. 6C). *Alveolina* and echinoderm fragments also occur.

Micrite and oligotypic fauna dominated by miliolids indicate deposition in a restricted lagoon.

MF9 *Alveolina* wackestone

Thin gray beds in the lower Ypresian limestone contain abundant *Alveolina* set in micrite (Fig. 6D). Common miliolids, echinoderm fragments, and small hyaline benthic foraminifera occur.

Micrite and oligotypic faunas dominated by *Alveolina* suggest deposition in a lagoonal environment slightly deeper than MF8.

MF10 Mudstone

Thin gray beds in the lower Ypresian limestone entirely consist of micrite (Fig. 6E).

Absence of bioclasts and laminations indicates a low-energy lagoonal environment.

MF11 Ostracod wackestone

Thin gray beds in the middle Ypresian limestone are dominated by ostracods set in micritic matrix (Fig.6F).

Micrite and oligotypic ostracod fauna suggest deposition in a restricted brackish/schizohaline lagoon.

MF12 Bivalve wackestone

Thin gray beds in the middle Ypresian limestone are wackestones rich in large bivalves (oysters) with small miliolids, ostracods, and echinoderm fragments (Fig. 6G).

Oysters and miliolids in micritic matrix suggest a restricted lagoon environment.

MF13 Bioclastic wackestone

Thin gray beds in the upper Ypresian limestone contain *Alveolina*, small hyaline benthic foraminifera, miliolids, ostracods, gastropods, green algae, and echinoderms set in micritic matrix (Fig. 6H).

Micrite and diverse bioclasts indicate deposition in a shallow-marine environment with moderate circulation and wave energy.

3.4 Carbon and oxygen isotopes

Although the upper Thanetian limestone is characterized by fairly stable $\delta^{13}C$ values centered around 2‰, a slight negative spike, maintained over a stratal thickness of ~1.2 m, was detected ~1 m below the main carbon-isotope excursion (CIE; Fig. 7). This pre-onset excursion (POE; Bowen et al., 2014) – previously identified in many terrestrial records (Magioncalda et al., 2004; Domingo et al., 2009; Bowen et al., 2014) but only uncertainly in marine strata (Zachos et al., 2006; Luciani et al., 2007; John et al., 2008; Zamagni et al., 2012; Sef-Trail et al., 2012) – is thought to document a perturbation of the carbon exogenic pool prior to the main perturbation related to the PETM.

The onset of the main CIE is testified by an abrupt $\delta^{13}C$ decline from 0 to -6‰ at the base of the Claret Formation (Fig. 6). Negative $\delta^{13}C$ values around -6.5‰ are maintained up to the top of the Claret Formation, where they show a sharp decrease down to -10.4‰. The unconformable base of the Ypresian limestone marks the abrupt return to positive pre-excursion $\delta^{13}C$ values around +1‰.

4 Discussion

4.1 Environmental and relative sea-level changes

High-resolution microfacies analysis of the Campo section documents two transgressive episodes of carbonate-ramp sedimentation abruptly interrupted by siliciclastic supply during deposition of the Claret Formation (Fig. 7). The first deepening trend starts with algal packstone/rudstone (MF1) and foraminifera and algal grainstone (MF2) representing high-energy shoal deposits at the base of the upper Thanetian limestone, overlain by red algal bindstone (MF3) deposited in quiet, deeper-water environments (Fig.7). In the uppermost part of the unit, *Distichoplax* wackestone with *Microcodium* (MF4) and *Microcodium* packstone (MF5) indicate reworking of calcareous paleosols during sudden floods from the continent, thus heralding a major environmental change.

Subsequently, a forced regression documented by the unconformable base of the Claret Formation was overlain by greenish marlstones containing freshwater faunas (MF6a) interbedded with carbonates containing normal-marine faunas (MF6b). This indicates deposition in brackish to schizohaline paralic environments during a period of increased terrigenous supply and continental runoff.

The base of the Ypresian limestone documents renewed transgression, with deposition of miliolid packstone (MF8), *Alveolina* wackestone (MF9), mudstone (MF10), ostracod wackestone (MF11) and bivalve wackestone (MF12) in restricted lagoonal environments. The unit is eventually capped by shallow-marine bioclastic wackestone (MF13) (Fig.7).

4.2 The PETM record of the Campo carbonate platform

The original isotopic signature of shallow-marine carbonates may be modified – especially in meteoric environments – by diagenetic fluids, typically resulting in decreased $\delta^{13}C$ and $\delta^{18}O$ values. Microscope inspections, however, suggest good preservation of foraminifera and other fossils in the upper Thanetian and Ypresian limestones exposed in the Campo section. In the $\delta^{13}C$–$\delta^{18}O$ cross-plot, data cluster in an area that indicates water-rock interaction within a closed system (Banner and Hanson, 1990). This implies that, although the $\delta^{18}O$ values were altered, the primary $\delta^{13}C$ values were retained. In the Claret Formation, extremely negative values of -5.1‰ to -10.5‰ may be the result of meteoric influx and terrigenous supply.

The International Commission on Stratigraphy defined the P/E boundary as corresponding to the onset of the CIE in the hemipelagic strata at the Global Stratotype Section and Point in the Dababiya Quarry of Egypt (Aubry et al., 2007). Although the Campo section is a classic shallow marine PETM locality, the onset of the PETM has here remained undecided. Schmitz and Pujalte (2003) suggested two possibilities: a) the sharp base of the Claret Formation (Orue-Etxebarria et al., 2001); b) the top of member 2 of the Claret Formation. Pujalte et al. (2009, 2014) and Manners et al. (2013), instead, indicated the base of conglomerate-bearing member 2 of the Claret Formation, based on field mapping, biostratigraphy, and carbonate $\delta^{13}C$ data, thus implying a time-lag between the environmental change and the isotopic response (Duller et al., 2019)

Our higher-resolution carbonate $\delta^{13}C$ data suggest that the timing of the CIE onset in the Campo section is different from what put forward by previous workers. Based on coupled larger-benthic-foraminifera and carbon-isotope stratigraphy, we demonstrate that the PETM onset corresponds to the unconformable base of the Claret Formation and is maintained over the entire thickness of the unit, unconformably overlain in turn by the Ypresian limestone deposited after the PETM recovery.

Foraminiferal assemblages of SBZ4/SBZ5 found below the Claret Formation are replaced by SBZ6 assemblages above, indicating that significant hiatus are involved with the unconformities bracketing the Claret Formation. This unit, therefore, records only the core of the CIE, whereas the record of the PETM onset and PETM recovery went lost at the unconformities below and above.

4.3 The demise of the carbonate ramp in response to PETM warming

It is usually very difficult to distinguish the relative influence of tectonics, eustasy, and climate on the evolution of a carbonate system. Marginal-marine sedimentary records from the North Atlantic continental margin (John et al., 2008; Sluijs et al., 2008), US Gulf Coastal Plain (Sluijs et al., 2014), Pacific (John et al., 2008; Sluijs et al., 2008), western Tethys (Gavrilov et al., 2003;

Speijer and Morsi, 2002; Speijer and Wagner, 2002), Arctic Ocean (Handley et al., 2011), and Turgay Strait of northern Kazakhstan (Iakovleva et al., 2001) indicate that the PETM onset correponds to a sea-level rise. The lacunose stratigraphic record of the Campo section, instead, indicates a forced regression at the base of the Claret Formation, possibly related to local tectonic uplift during ongoing Pyrenean deformation. Other factors may be involved as well.

In marginal marine sites worldwide (e.g., Bolle and Adatte, 2001; Hollis et al., 2005; John et al., 2008), the PETM has been shown to correspond to marked hydrological changes. In the mid-latitude Pyrenees, climate became more seasonally extreme, with brief but intense wet seasons separated by a prolonged dry season (Schmitz and Pujalte, 2003, 2007). Water discharge is reckoned to have increased by at least 30% and potentially by as much as an order of magnitude during the early PETM phase in northern Spain (Chen et al., 2018). Consequently, the hydrological cycle and rock weathering increased notably during the PETM in the Pyrenean hinterland, which resulted in intensified siliciclastic supply to the Tremp-Graus basin, and the temporary demise of the Campo carbonate ramp. Increased siliciclastic supply triggered by the intensified magnitude and frequency of extreme rainfall and runoff events may have led to the concomitant regression.

A similar demise of carbonate platforms resulting from increased terrigenous supply during the PETM has been documented from marginal marine sites around the world. In the Ordesa-Monte Perdido National Park, Pujalte et al. (2016) reported that continental quartzose pebbly sandstones abruptly overlie an erosional surface carved into upper Thanetian marine carbonates and are overlain in turn by lower Ypresian marine limestone. In southern Tibet, a siliciclastic interval is bracketed between Thanetian middle ramp sediments with *Lockhartia*, *Daviesina*, *Miscellanea* and *Orbitosiphon* and Ypresian lagoonal carbonates with *Nummulites* and *Alveolina* (Jiang et al., 2020). In the Galala platform of Egypt, pure carbonate ramp deposits of Paleocene age change upwards to mixed carbonate-siliciclastic deposits in the early Eocene, also testifying to a temporary crisis of the carbonate platform (Höntzsch et al., 2011).

5 Conclusion

We have illustrated new sedimentological, biostratigraphic, and carbon-isotope data on upper Paleocene to lower Eocene strata exposed in the classical Campo section of the Spanish Pyrenees to reassess environmental changes across the PETM. The pre-PETM upper Thanetian limestone represents transgressive inner ramp sediments followed by a sudden change to siliciclastic-influenced deposition in the syn-PETM Claret Formation, followed in turn by renewed carbonate-ramp sedimentation of the post-PETM lower Ypresian limestone.

The pre-onset excursion (POE) is well documented at the top of upper Thanetian limestone but, unfortunately, the record of the early development of the PETM event is lost in the unconforrmity that caps the unit. As we discovered in our previous article (Li et al., in press) on the Shenkezha section in Tingri area, southern Tibet, the isotopically defined P/E boundary, does not match the biostratigraphically defined horizon, but would do so if the P/E boundary were to be placed at the end of, rather than at the onset of the CIE. The PETM core is well testified in the overlying marls of the Claret Formation and maintained throughout this 10 m-thick unit. The PETM recovery is however lost again in the unconformity above, followed by the return to normal $\delta^{13}C$ values of ~1 ‰ at the base of the lower Ypresian limestone. The temporary demise of the Campo carbonate ramp during the early PETM and abrupt transition to brackish paralic environments characterized by increased terrigenous supply is ascribed to a drastic change in climate and regional hydrology caused by a notable increase in the magnitude and frequency of extreme rainfall and runoff events.

Acknowledgments

We are grateful to Roi Silva-Casal and Beñat Intxauspe-Zubiaurre for their precious assistance in the field. We thank Haiyan Shen for assistance in the laboratory, and Jingxin Jiang and Xinyu Liu for their help in sample preparation. This study was financially supported by the National Natural Science Foundation of China (41888101, 41702105) and by MIUR – Dipartimenti di Eccellenza 2018–2022, Department of Earth and Environmental Sciences, University of Milano-Bicocca.

References

Aubry, M.-P., Ouda, Kh., Dupuis, C., Berggren, W.A., Van Couvering, J.A., the Members of the Working Group on the Paleocene/Eocene Boundary, 2007. Global Standard Stratotype Section and Point (GSSP) for the base of the Eocene Series in the Dababiya Section (Egypt). Episodes 30, 271-286.

Beavington-Penney, S.J., Racey, A., 2004. Ecology of extant nummulitids and other larger benthic foraminifera: application in palaeoenvironmental analysis. Earth-Science Reviews 67, 219-265.

BouDagher-Fadel, MK, (2008). Evolution and Geological Signifi cance of Larger Benthic Foraminifera: Developments in Paleontology and Stratigraphy, Volume 21: Amsterdam, Elsevier.

Bolle, M. P., and Adatte T., 2001. Palaeocene-early Eocene climatic evolution in the Tethyan realm: Clay mineral evidence, Clay Miner. 36, 249-261

Carmichael, M.J., Inglis, G.N., Badger, M.P.S., Naafs, B.D.A., Behrooz, L., Remmelzwaal, S., Monteiro, F.M., Rohrssen, M., Farnsworth, A., Buss, H.L., Dickson, A.J., Valdes, P.J., Lunt, D.J., Pancost, R.D., 2017. Hydrological and associated biogeochemical consequences of rapid global warming during the Paleocene-Eocene Thermal Maximum. Global and Planetary Change 157, 114-138.

Chen et al. (2018)

Duller, R.A., Armitage, J.J., Manners, H.R., Grimes, S., Dunkley Jones, T., 2019. Delayed sedimentary response to abrupt climate change at the Paleocene-Eocene boundary, northern Spain. Geology 47, 159-162.

Dunham, R.J., 1962. Classification of carbonate rocks according to depositional textures. AAPG Mem. 1, 108-121.

Dunkley Jones, T., Lunt, D.J., Schmidt, D.N., Ridgwell, A., Sluijs, A., Valdes, P.J., Maslin, M., 2013. Climate model and proxy data constraints on ocean warming across the Paleocene–Eocene Thermal Maximum. Earth-Science Reviews 125, 123-145.

Embry, A.F., Klovan, J.E., 1971. A late Devonian reef tract on northeastern Banks Island, NWT. Bull. Can. Petrol. Geol. 19, 730-781.

Flügel, E., 2010. Microfacies of Carbonate Rocks: Analysis, Interpretation and Application. second ed. Springer-Verlag, Berlin Heidelberg New York.

Fernández, O., Muñoz, J.A., Arbués, P., Falivene, O., 2012. 3D structure and evolution of an oblique system of relaying folds: the Ainsa basin (Spanish Pyrenees). J. Geol. Soc. 169, 545-559.

Ford, M., Hemmer, H., Vacherat, A., Gallagher, K., Christophoul, F., 2016. Retro-Wedge Foreland Basin Evolution along the ECORS Line, Eastern Pyrenees, France . Journal of the Geological Society 173, 419-37.

Gavrilov, Y.O., Shcherbinina, E.A., Oberhänsli, H., 2003. Paleocene-Eocene boundary events in the northeastern peri-Tethys. Geological Society of America Special Paper 369, 147-168.

Gutjahr, M., Ridgwell, A., Sexton, P.F., Anagnostou, E., Pearson, P.N., Palike, H., Norris, R.D., Thomas, E., Foster, G.L., 2017. Very large release of mostly volcanic carbon during the

Palaeocene-Eocene Thermal Maximum. Nature 548, 573-577.

Gradstein, F.M., Ogg, J.G., Schmitz, M.D., Ogg, G.M., 2012. The Geologic Time Scale 2012. Elsevier, Amsterdam.

Handley, L., Crouch, E.M., Pancost, R.D., 2011. A New Zealand record of sea level rise and environmental change during the Paleocene–Eocene Thermal Maximum. Palaeogeography, Palaeoclimatology, Palaeoecology 305, 185-200.

Hottinger, L, 1960. Uber Eocane und Paleocane Alveolinen. Eclogae Geol Helv 53, 265-283

Höntzsch, S., Scheibner, C., Guasti, E., Kuss, J., Marzouk, A.M., Rasser, M.W., 2011. Increasing restriction of the Egyptian shelf during the Early Eocene? — New insights from a southern Tethyan carbonate platform. Palaeogeography, Palaeoclimatology, Palaeoecology 302, 349-366.

Hollis, C. J., G. R. Dickens, B. D. Field, C. M. Jones, and C. Percy Strong (2005), The Paleocene-Eocene transition at Mead Stream, New Zealand: A southern Pacific record of early Cenozoic global change, Palaeogeogr. Palaeoclimatol. Palaeoecol. 215, 313-343

Iakovleva, A. I., Brinkhuis, H., and Cavagnetto, C.: Late Palaeocene-Early Eocene dinoflagellate cysts from the Turgay Strait, Kazakhstan; correlations across ancient seaways, Palaeogeogr. Palaeocl., 172, 243-268, 2001

John, C.M., Bohaty, S.M., Zachos, J.C., Sluijs, A., Gibbs, S., Brinkhuis, H., Bralower, T.J., 2008. North American continental margin records of the Paleocene-Eocene thermal maximum: Implications for global carbon and hydrological cycling. Paleoceanography, 23, PA2217, doi:10.1029/2007PA001465

Jiang, J., Hu, X., Li, J., BouDagher-Fadel, M., Garzanti, E., 2020. Enhanced hydrological change during the Paleocene-Eocene thermal maximum (PETM) recorded in shallow-marine Xigaze forearc basin (southern Tibet). Palaeogeography Palaeoclimatology Palaeoecology, underview.

Kabanov, P., Anadón, P., Krumbein, W.E., 2008. Microcodium: an extensive review and a proposed non-rhizogenic biologically induced origin for its formation. Sedimentary Geology, 205(3-4), 79-99.

Košir, A., 2004. Microcodium revisited: root calcification products of terrestrial plants on carbonate-rich substrates. Journal of Sedimentary Rresearch, 74(6), 845-857.

Li, J., Hu, X., Garzanti, E., BouDagher-Fadel, M., 2017. Shallow-water carbonate responses to the Paleocene-Eocene thermal maximum in the Tethyan Himalaya (southern Tibet): Tectonic and climatic implications. Palaeogeography Palaeoclimatology Palaeoecology 466, 153-165.

Luciani, V., Giusberti, L., Agnini, C., Backman, J., Fornaciari, E., Rio, D., 2007. The Paleocene–Eocene thermal maximum as recorded by Tethyan planktonic foraminifera in the Forada section (northern Italy). Marine Micropaleontology, 64(3-4), 189-214.

Manners, H.R., Grimes, S.T., Sutton, P.A., Domingo, L., Leng, M.J., Twitchett, R.J., Hart, M.B., Dunkley Jones, T., Pancost, R.D., Duller, R., Lopez-Martinez, N., 2013. Magnitude and profile of organic carbon isotope records from the Paleocene–Eocene Thermal Maximum: Evidence from northern Spain. Earth and Planetary Science Letters 376, 220-230.

McInerney, F.A., Wing, S.L., 2011. The Paleocene-Eocene Thermal Maximum: A Perturbation of Carbon Cycle, Climate, and Biosphere with Implications for the Future, Annual Review of Earth and Planetary Sciences 39, 489-516.

Molina, E., Angori, E., Arenillas, I., Brinkhuis, H., Crouch, E.M., Luterbacher, H., Monechi, S., Schmitz, B., 2003. Correlation between the Paleocene/Eocene boundary and the Ilerdian at Campo, Spain. Revue de Micropaléontologie 46, 95-109.

Orue-Etxebarria, X., Pujalte, V., Bernaola, G., Apellaniz, E., Baceta, J.I., A. Payros, Nuñez-Betelu, K., Serra-Kiel, J., Tosquella, J., 2001. Did the Late Paleocene thermal maximum affect the evolution of larger foraminifers? Evidence from calcareous plankton of the Campo Section (Pyrenees, Spain). Marine Micropaleontology 2001, 45-71.

Payros et al., 2000.

Pujalte, V., Schmitz, B., Baceta, J.I., Orue-Etxebarria, X., Bernaola, G., Dinares-Turell, J., Payros, A., Apellaniz, E., Caballero, F., 2009. Correlation of the Thanetian-Ilerdian turnover of larger foraminifera and the Paleocene-ocene thermal maximum:confirming evidence from the Campo area (Pyrenees, Spain). Geologica Acta 7, 161-175.

Pujalte et al., 2009b. Redefinition of the Ilerdian Stage (early Eocene). Geologica Acta 7, 177-194.

Pujalte, V., Schmitz, B., Baceta, J.I., 2014. Sea-level changes across the Paleocene–Eocene interval in the Spanish Pyrenees, and their possible relationship with North Atlantic magmatism. Palaeogeography, Palaeoclimatology, Palaeoecology 393, 45-60.

Pujalte, V., Robador, A., Payros, A., Maria Samso, J., 2016. A siliciclastic braid delta within a lower Paleogene carbonate platform (Ordesa-Monte Perdido National Park, southern Pyrenees, Spain): Record of the Paleocene–Eocene Thermal Maximum perturbation. Palaeogeography, Palaeoclimatology, Palaeoecology 459, 453-470.

Pujalte, V., Monechi, S., Ortíz, S., Orue-Etxebarria, X., Rodríguez-Tovar, F., Schmitz, B., 2019. Microcodium-rich turbidites in hemipelagic sediments during the Paleocene–Eocene Thermal Maximum: Evidence for extreme precipitation events in a Mediterranean climate (Río Gor section, southern Spain). Global and Planetary Change, 178, 153-167.

Roest, W.R., Srivastava, S.P., 1991. Kinematics of the plate boundaries between Eurasia, Iberia, and Africa in the North Atlantic from the Late Cretaceous to the present. Geology 19, 613-616.

Sarkar, S., 2018. The enigmatic Palaeocene-Eocene coralline Distichoplax: Approaching the structural complexities, ecological affinities and extinction hypotheses. Marine Micropaleontology 139, 72-83.

Scheibner, C., Rasser, M.W., Mutti, M., 2007. The Campo section (Pyrenees, Spain) revisited: Implications for changing benthic carbonate assemblages across the Paleocene–Eocene boundary. Palaeogeography, Palaeoclimatology, Palaeoecology 248, 145-168.

Scheibner, C., Speijer, R.P., Marzouk, A.M., 2005. Turnover of larger foraminifera during the Paleocene-Eocene Thermal Maximum and paleoclimatic control on the evolution of platform ecosystems. Geology 33, 493-496.

Schmitz, B., Pujalte, V., 2003. Sea-level, humidity, and land-erosion records across the initial Eocene thermal maximum from a continental-marine transect in northern Spain. geology 31, 689-692.

Schmitz, B., Pujalte, V., 2007. Abrupt increase in seasonal extreme precipitation at the Paleocene-Eocene boundary. Geology 35, 215-218.

Self−Trail, J. M., Powars, D. S., Watkins, D. K., Wandless, G. A., 2012. Calcareous nannofossil assemblage changes across the Paleocene−Eocene thermal maximum: Evidence from a shelf setting. Marine Micropaleontology 92-93, 61-80

Serra-Kiel, J., Hottinger, L., Caus, E., Drobne, K., Ferrandez, C., Jauhri, A. K., Less, G., Pavlovec, R., Pignatti, J., Samso, M.J., Schaub, H., Sirel, E., Strougo, A., Tambaregu, Y., Tosquella, J., Zakrevskaya, E., 1998. Larger foraminifera biostratigraphy of the Tethyan Paleocene and Eocene. Bull. Soc. géol.France 169 (2), 281-299.

Sluijs, A., Brinkhuis, H., Crouch, E.M., John, C.M., Handley, L., Munsterman, D., Bohaty, S.M., Zachos, J.C., Reichart, G.-J., Schouten, S., Pancost, R.D., Damsté, J.S.S., Welters, N.L.D., Lotter, A.F., Dickens, G.R., 2008. Eustatic variations during the Paleocene-Eocene greenhouse world. Paleoceanography 23, PA4216, doi:10.1029/2008PA001615.

Sluijs, A., van Roij, L., Harrington, G.J., Schouten, S., Sessa, J.A., LeVay, L.J., Reichart, G.J., Slomp, C.P., 2014. Warming, euxinia and sea level rise during the Paleocene–Eocene Thermal Maximum on the Gulf Coastal Plain: implications for ocean oxygenation and nutrient cycling. Climate of the Past 10, 1421-1439.

Speijer, R.P., Wagner, T., 2002. Sea-level changes and black shales associated with the late Paleocene thermal maximum: Organic-geochemical and micropaleontologic evidence from the southern Tethyan margin (Egypt-Israel). Geological Society of America Special Paper 356, 533-549.

Trenberth, K. E., (2011). Changes in precipitation with climate change, Clim. Res., 47, 1-16.

Zachos, J.C., Bohaty, M.W.W.S., Delaney, M.L., Brill, M.R.P.A., Bralower, T.J., Premoli-Silva, I., 2003. A Transient Rise in Tropical Sea Surface Temperature During the Paleocene-Eocene Thermal Maximum. Science 302, 1551-1554.

Zachos, J.C., Roh, U., Schellenberg, S.A., Sluijs, A., Hodell, D.A., Kelly, D.C., Thomas, E., Nicolo, M., Raffi, I., Lourens, L.J., McCarren, H., Kroon, D., 2005. Rapid Acidification of the ocean During the Paleocene-Eocene Thermal Maximum. Science 308, 1611-1615.

Zamagni, J., Mutti, M., Ballato, P., Kosir, A., 2012. The Paleocene-Eocene thermal maximum (PETM) in shallow-marine successions of the Adriatic carbonate platform (SW Slovenia). Geological Society of America Bulletin 124, 1071-1086.

Zeebe, R.E., Ridgwell, A., Zachos, J.C., 2016. Anthropogenic carbon release rate unprecedented during the past 66 million years. Nature Geoscience 9, 325-329.

Zhang, Q., Willems, H., Ding, L., 2013. Evolution of the Paleocene-Early Eocene larger benthic foraminifera in the Tethyan Himalaya of Tibet, China. International Journal of Earth Sciences 102, 1427-1445.

Figure captions

Fig.1 Late Paleocene-early Eocene paleogeographic sketch map of the Pyrenean domain showing the location of the Campo section in northern Spain (modified from Schmitz and Pujalte, 2003).

Fig.2 Field photographs of the Campo section. A) Full view of the studied Paleocene-Eocene interval; (B) thick-bedded upper Thanetian limestone; C, D) sharp surface between the upper

Thanetian limestone and the Claret Formation showing gastropod moulds; E) thin-bedded sandy limestone in the Claret formation; F, G) thin- to thick-bedded lower Ypresian limestone.

Fig.3 Distribution of larger benthic foraminifera in the Campo section (northern Spain).

Fig.4 Larger benthic foraminifera assemblages in the Campo section. A) *Glomalveolina levis* Hottinger, sample 18CP11; B-C) *Miscellanea miscella* (d'Archiac and Haime, 1853), B) sample 18CP19, C) sample 18CP14; D) a) *Daviesina sp.*, b) *Rotospirella conica* (Smout), c) Rodophyte sp., sample 18CP09; E) *Distichoplax biserialis* (Dietrich), sample 19CP06; F) *Opertorbitolites gracilis* (Lehmann), sample 18CP38; G) *Alveolina globula* Hottinger, sample 18CP38; H) *Alveolina pasticillata* Schwager, sample 18CP40; I) *Alveolina aragonensis* Hottinger, sample 18CP41; J) *Alveolina globosa* (Leymerie), sample 18CP41. Scale bar: A, 0.15 mm; B-D), 0.5 mm; E-J), 1 mm.

Fig.5 Micrographs of microfacies MF1 to MF6 in the Campo section. A) Sandy red algal packstone (MF1), sample 18CP18; B) foraminiferal and algal grainstone (MF2), sample 18CP14; C) red algal bindstone (MF3), sample 18CP09; D) *Distichoplax* wackestone (MF4), sample 18CP05; E) the contact between MF4 and MF5, sample 18CP02; F) *Microcodium* packstone with miliolids (MF5), sample 18CP01; G) Marlstone (MF6a), sample 18CP25; H) Sandy rudstone (MF6b), sample 18CP53; q, quartz; gc, geniculate coralline algae; bf, benthic foraminifera; cc, crustose coralline algae; b, bryozoan; db, *distichoplax biserialis*; mi, miliolid; m, microcodium.

Fig.6 Micrographs of microfacies MF6 to MF13 in the Campo section. A) Sandy mudstone (MF6c), sample 18CP56; B) Small benthic foraminiferal wackestone with ostracods (MF7); C) *Miliolids* packstone (MF8), sample 18CP38; D) *Alveolina* wackestone (MF9), sample 18CP41; E) Mudstone (MF10), sample 18CP43; F) Ostracod wackestone (MF11), sample 18CP45; G) Bivalve wackestone (MF12), sample 18CP46; H) Bioclastic wackestone (MF13), sample 18CP47. q, quartz; mi, miliolid; a, alveolinid; os, ostracod; b, bivalve; da, dasyclade algae

Fig.7 Stratigraphic log indicating microfacies, water-depth, sedimentary environment, and carbonate $\delta^{13}C$ curve in the Campo section. The reconstructed changes in environment and relative sea level across the PETM are shown.

Fig.8 Paleogeographic and paleoenvironmental sketch maps of the Campo section (northern Spain).

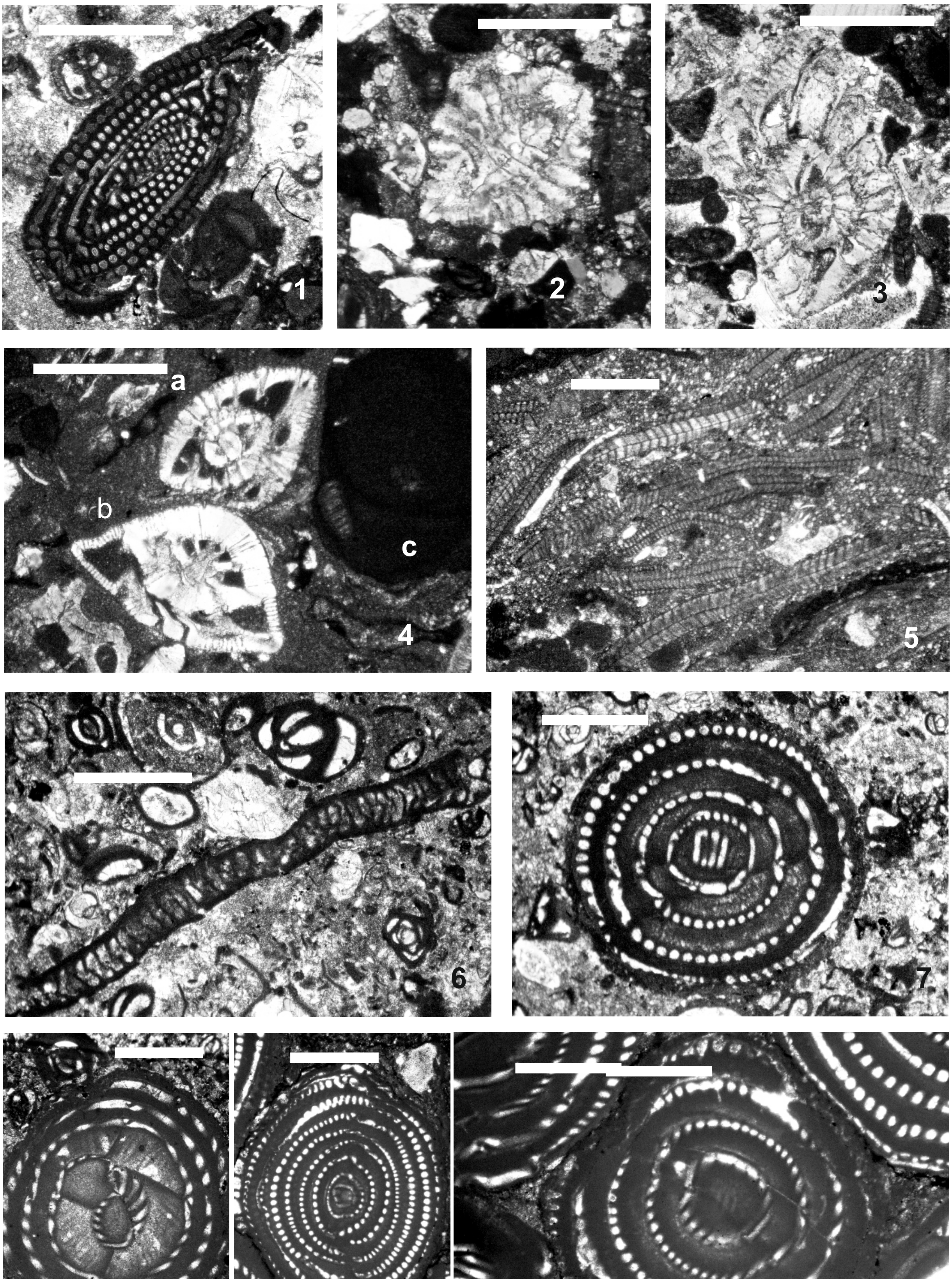
1
2
3
a
b
c
4
5
6
7
8
9
10